
Optimizing Sampling Patterns for Compressed Sensing MRI with Diffusion Generative Models

Sriram Ravula

University of Texas at Austin
Electrical and Computer Engineering
sriram.ravula@utexas.edu

Brett Levac

University of Texas at Austin
Electrical and Computer Engineering
blevac@utexas.edu

Ajil Jalal

University of California, Berkeley
Electrical Engineering and Computer Sciences
ajiljalal@berkeley.edu

Jonathan I. Tamir

University of Texas at Austin
Electrical and Computer Engineering
jtamir@utexas.edu

Alexandros G. Dimakis

University of Texas at Austin
Electrical and Computer Engineering
dimakis@austin.utexas.edu

Abstract

Diffusion-based generative models have been used as powerful priors for magnetic resonance imaging (MRI) reconstruction. We present a learning method to optimize sub-sampling patterns for compressed sensing multi-coil MRI that leverages pre-trained diffusion generative models. Crucially, during training we use a single-step reconstruction based on the posterior mean estimate given by the diffusion model and the MRI measurement process. Experiments across varying anatomies, acceleration factors, and pattern types show that sampling operators learned with our method lead to competitive, and in the case of 2D patterns, improved reconstructions compared to baseline patterns. Our method requires as few as five training images to learn effective sampling patterns.

1 Introduction

Compressed sensing (CS) [11, 15] is a powerful framework for recovering a structured signal from a limited number of measurements, with applications in many imaging inverse problems. In particular, CS has been used to accelerate magnetic resonance imaging (MRI) beyond the Nyquist rate by sampling a pseudo-random subset of Fourier coefficients in k-space and imposing a sparse prior on the image [33]. In the multi-coil setting, CS-MRI can be combined with parallel imaging [40, 36, 17] to exploit additional structure. While the incoherence condition in CS-MRI is typically realized through pseudo-random sampling, optimal recovery for parallel imaging is based on linear predictability from local neighborhoods in k-space [18]. Thus, there is a tradeoff in balancing random and structured sampling.

More recently, deep learning has been used as a powerful tool to solve ill-posed inverse problems beyond the capabilities of sparsity priors, through either supervised or unsupervised deep neural

Code available at https://github.com/Sriram-Ravula/MRI_Sampling_Diffusion.

networks [34]. While these techniques have demonstrated unprecedented reconstruction quality for accelerated multi-coil MRI, the sub-sampling pattern is still typically chosen based on heuristics from CS or parallel imaging. Several approaches have been introduced to optimize the sampling pattern, either separately or jointly with the reconstruction network, through end-to-end learning [7, 2, 49, 39, 56, 3]. However, these approaches are only suitable when the gradient of the sampling operator can be calculated through the full reconstruction network. Thus, while these techniques have been very successful for optimizing the sampling pattern for end-to-end reconstruction networks such as the U-Net [54], Var-Net [19, 45], and other unrolled methods [1], it is unclear how to extend it to unsupervised methods such as CS with generative models (CSGM) proposed in [9] and applied to MRI in [24].

In this work we optimize the collected samples for CSGM MRI. We use the recently proposed unsupervised method of posterior sampling with diffusion models [24, 13, 32, 43], since it has been shown to be robust to changes in imaging anatomy, acceleration factor, and sub-sampling patterns, without requiring retraining. As these reconstructions are not amenable to algorithm unrolling, we propose a simple and effective alternative to the full gradient of the reconstruction network that can be used to optimize the selection of which samples to keep. We apply our approach to multi-coil Cartesian MRI and demonstrate that optimized sampling patterns can be used to reduce the reconstruction error for a given acceleration factor.

1.1 Contributions

- We propose a novel training objective for selecting which samples to obtain for MRI reconstruction using diffusion-based generative models. Our method is based on a theoretical result which provides a closed-form solution for calculating the mean of the posterior distribution.
- We use pre-trained diffusion models as priors without requiring further tuning, making our method modular. Our method is also independent of the choice of posterior sampling algorithm.
- We empirically demonstrate that our approach can learn competitive sampling patterns using as few as five training samples. Qualitative results show that patterns learned with our method lead to reconstructions with fewer artifacts than baseline equispaced and Poisson disc masks.

1.2 Related Work

Compressed Sensing with Generative Models The theory of compressed sensing [11, 15] demonstrates that a signal can be accurately recovered from measurements taken below the Nyquist rate, given that the signal is sparse in an appropriately-chosen basis. The authors of CSGM [9] extended this finding by showing that the range of a generative model is a more powerful prior than sparsity. Generative models have been used as priors for inverse problems in deblurring [53], phase retrieval [20], 1-bit compressed sensing [31, 37], and many more. Various reconstruction algorithms have been proposed to leverage generative models for these reconstruction tasks [42, 25, 6, 28, 44], including methods which use untrained models [47, 21] or models trained entirely on compressive measurements [10]. See the survey in [34] for taxonomy of image reconstruction algorithms and applications.

MRI Sampling Pattern Selection Previous works have looked at optimal sampling pattern selection for accelerated MRI [7, 55, 49, 50, 2, 30]. In each approach, the reconstruction network is trained in an end-to-end fashion jointly with the sampling mask. The learned sampling masks in these approaches were either treated as a probability density function to select points on the Cartesian grid, or as non-Cartesian coordinates in the non-uniform Fast Fourier Transform (NUFFT) which were subsequently treated as learnable parameters. Other works have taken an adaptive approach to selecting sampling patterns for individual patients [51].

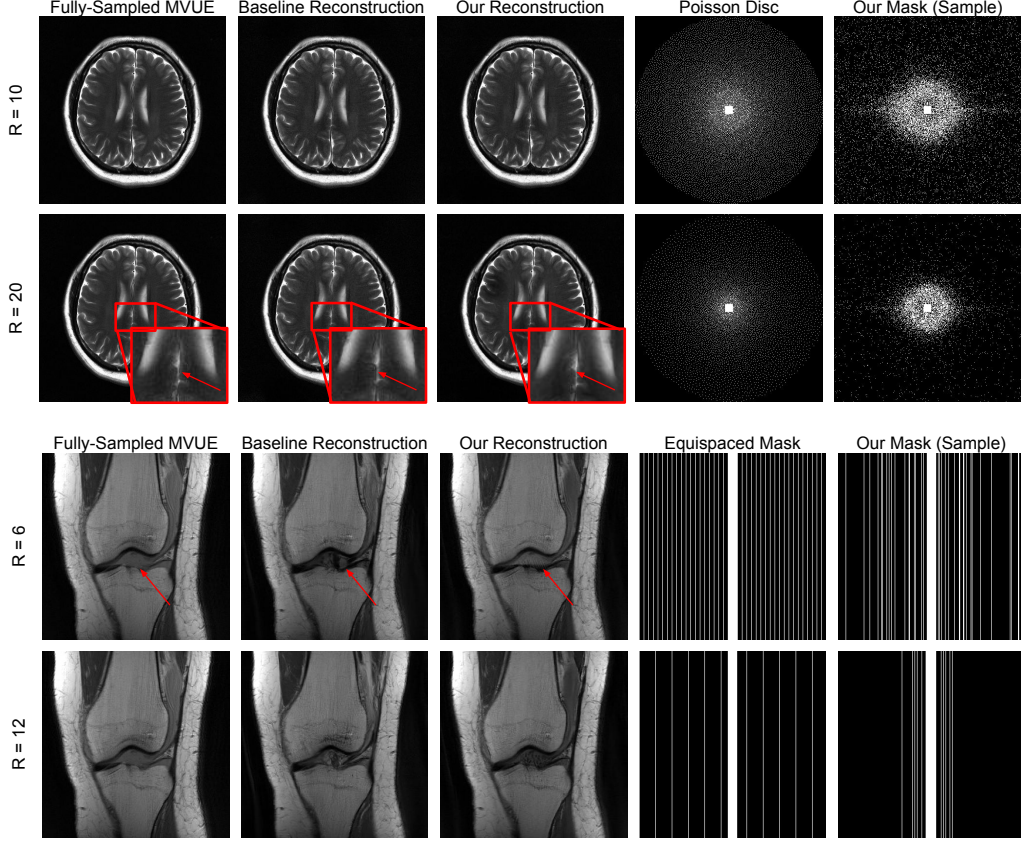


Figure 1: **Reconstructions using baseline masks vs masks learned with our method.** We perform posterior sampling using a diffusion model to reconstruct MRI scans using varying anatomies, pattern types, and acceleration factors (R). Artifacts in the reconstructions are highlighted with red arrows and insets (zoom may be needed). Masks learned with our method produce reconstructions with fewer artifacts.

2 Background

2.1 Diffusion-Based Generative Models

Diffusion-based models learn to generate new signals by reversing a corruption process. The two main classes of diffusion models, Score-Based Models (SBMs) [41] and Denoising Diffusion Probabilistic Models (DDPMs) [22], specifically are trained to remove Gaussian noise. The noise magnitude is determined by the variance σ_t^2 and indexed by time step $t \in [0, T]$. Typically, $\sigma_0^2 = 0$ and corresponds to clean signals, and σ_T^2 is chosen to be very large so that the distribution of noisy signals at time $t = T$ is indistinguishable from pure Gaussian noise.

Song et al. [44] unify the discrete-time noise processes of SBMs and DDPMs under the framework of continuous-time Stochastic Differential Equations (SDEs). They cast SBMs as reversing *Variance Exploding* (VE) SDEs, with noisy image distributions having increasing variance as t increases, and DDPMs as reversing *Variance Preserving* (VP) SDEs, whose noisy image distributions typically maintain unit variance throughout the diffusion process. In this paper, we focus on the VE-SDE framework.

The noisy signal at time t in the forward diffusion process is given by $\mathbf{x}_t \in \mathbb{R}^n$. The diffusion process is modeled as the solution to an Itô SDE of the form

$$d\mathbf{x} = \mathbf{f}(\mathbf{x}, t)dt + g(t)d\mathbf{w}. \quad (1)$$

Here, \mathbf{w} is the standard n -dimensional Wiener process, and in the VE case, $\mathbf{f}(\mathbf{x}, t) = \mathbf{0}$ and $g(t) = \sqrt{\frac{d\sigma_t^2}{dt}}$. The variance σ_t^2 is a monotonically increasing function that defines the distribution of the diffused signal, with the property that at time $t = 0$ we recover the data distribution: $\mathbf{x}_0 \sim p_0 = p_{data}$. The goal of Diffusion-based models is to start from samples $\mathbf{x}_T \sim p_T$ consisting of pure Gaussian noise and reverse the forward diffusion given by Eq. (1) to arrive at samples $\mathbf{x}_0 \sim p_0$. Conveniently, the reverse of the forward SDE is also an SDE [4], with the form:

$$d\mathbf{x} = [\mathbf{f}(\mathbf{x}, t) - g(t)^2 \nabla_{\mathbf{x}_t} \log p_t(\mathbf{x}_t)]dt + g(t)d\bar{\mathbf{w}}, \quad (2)$$

where dt is now a negative time step and $\bar{\mathbf{w}}$ is the standard Wiener process when time flows backward. The reverse SDE depends on the *score function* $\nabla_{\mathbf{x}_t} \log p_t(\mathbf{x}_t)$ of the marginal distribution at time t .

A result from Vincent [48] states that we can learn the *unconditional* score function in Eq(1) through denoising score matching (DSM). DSM only requires the score of the *conditional* noise distribution at time t , which is known in closed-form for additive Gaussian noise. The training objective is

$$\theta^* = \underset{\theta}{\operatorname{argmin}} \mathbb{E}_{t \sim U[0, T]} [\lambda_t \mathbb{E}_{(\mathbf{x}_0, \mathbf{x}_t) \sim p_0(\mathbf{x}_0)p_t(\mathbf{x}_t|\mathbf{x}_0)} \|\mathbf{s}_\theta(\mathbf{x}_t, t) - \nabla_{\mathbf{x}_t} \log p_t(\mathbf{x}_t|\mathbf{x}_0)\|^2], \quad (3)$$

where λ_t is a time-dependent positive weighting function and $\mathbf{s}_\theta(\mathbf{x}_t, t)$ is the *score network*. Given enough data and model capacity, the score network learns to approximate the unconditional score function: $\mathbf{s}_\theta(\mathbf{x}_t, t) \simeq \nabla_{\mathbf{x}_t} \log p_t(\mathbf{x}_t)$. Subsequently, sampling with the score network is a matter of substituting $\mathbf{s}_\theta(\mathbf{x}_t, t)$ for the score function in Eq(2), then solving the reverse SDE.

2.2 Inverse Problems

In the inverse problem setting, we are given measurements of the form $\mathbf{y} = \mathcal{A}(\mathbf{x}_0) + \epsilon$, where $\mathcal{A} : \mathbb{R}^n \rightarrow \mathbb{R}^m$ is a known forward operator, $\epsilon \in \mathbb{R}^m$ is some additive noise, and $\mathbf{x}_0 \in \mathbb{R}^n$ is a signal we want to recover. The measurements are usually compressive, i.e. $m < n$, which means that there are infinitely many solutions that match the observed measurements. We turn to a Bayesian approach to find a solution.

Bayes' rule gives the relationship between the *prior* distribution $p(\mathbf{x})$ and the *posterior* distribution $p(\mathbf{x}|\mathbf{y})$ as $p(\mathbf{x}|\mathbf{y}) = p(\mathbf{x})p(\mathbf{y}|\mathbf{x})/p(\mathbf{y})$. If we take the gradient w.r.t. \mathbf{x} of the log of both sides, we find that

$$\nabla_{\mathbf{x}} \log p(\mathbf{x}|\mathbf{y}) = \nabla_{\mathbf{x}} \log p(\mathbf{x}) + \nabla_{\mathbf{x}} \log p(\mathbf{y}|\mathbf{x}). \quad (4)$$

Returning to the SDE framework, we can sample from the posterior distribution by using Eq.(4) in place of the score in Eq.(2):

$$d\mathbf{x} = [\mathbf{f}(\mathbf{x}, t) - g(t)^2 (\nabla_{\mathbf{x}_t} \log p_t(\mathbf{x}_t) + \nabla_{\mathbf{x}_t} \log p_t(\mathbf{y}|\mathbf{x}_t))]dt + g(t)d\bar{\mathbf{w}}. \quad (5)$$

Therefore, we need to know the score of the prior, $\nabla_{\mathbf{x}_t} \log p_t(\mathbf{x}_t)$, and the likelihood, $\nabla_{\mathbf{x}_t} \log p_t(\mathbf{y}|\mathbf{x}_t)$. To find the score of the prior distribution, we can train a diffusion model as described in Sec2.1. Unfortunately, the time-dependent likelihood $p_t(\mathbf{y}|\mathbf{x}_t)$ is not easy to obtain. In graphical terms, $\mathbf{x}_0 \rightarrow \mathbf{y}$ and $\mathbf{x}_0 \rightarrow \mathbf{x}_t$, but there is no closed-form dependency between the measurements \mathbf{y} and the noisy signal \mathbf{x}_t .

The authors of Diffusion Posterior Sampling (DPS) [12] propose to approximate $\nabla_{\mathbf{x}_t} \log p_t(\mathbf{y}|\mathbf{x}_t)$ by exploiting a result from Tweedie [16]. Tweedie's formula gives a closed-form expression for the mean of $p_0(\mathbf{x}_0|\mathbf{x}_t)$ when $p_t(\mathbf{x}_t|\mathbf{x}_0)$ belongs to an exponential family distribution. For the case of VE diffusions, we have that $p_t(\mathbf{x}_t|\mathbf{x}_0) = \mathcal{N}(\mathbf{x}_t; \mathbf{x}_0, \sigma_t^2 \mathbf{I})$, with the posterior mean given by Tweedie as

$$\hat{\mathbf{x}}_0 := \mathbb{E}_{\mathbf{x}_t \sim p_t(\mathbf{x}_t|\mathbf{x}_0)} [\mathbf{x}_0|\mathbf{x}_t] = \mathbf{x}_t + \sigma_t^2 \nabla_{\mathbf{x}_t} \log p_t(\mathbf{x}_t). \quad (6)$$

This formula allows us to get a "one-step" denoised estimate of the clean signal \mathbf{x}_0 using only the noisy signal \mathbf{x}_t and the score of the unconditional distribution, $\nabla_{\mathbf{x}_t} \log p_t(\mathbf{x}_t)$. We can replace the unconditional score in Eq.(6) using our trained score network $\mathbf{s}_\theta(\mathbf{x}_t, t)$ to approximate the posterior mean as

$$\hat{\mathbf{x}}_0 := \mathbb{E}_{\mathbf{x}_t \sim p_t(\mathbf{x}_t|\mathbf{x}_0)} [\mathbf{x}_0|\mathbf{x}_t] = \mathbf{x}_t + \sigma_t^2 \mathbf{s}_\theta(\mathbf{x}_t, t). \quad (7)$$

Assuming the forward operator \mathcal{A} is differentiable, DPS approximates the time-dependent score of the likelihood as

$$\nabla_{\mathbf{x}_t} \log p_t(\mathbf{y}|\mathbf{x}_t) \simeq \nabla_{\mathbf{x}_t} \log p_t(\mathbf{y}|\hat{\mathbf{x}}_0). \quad (8)$$

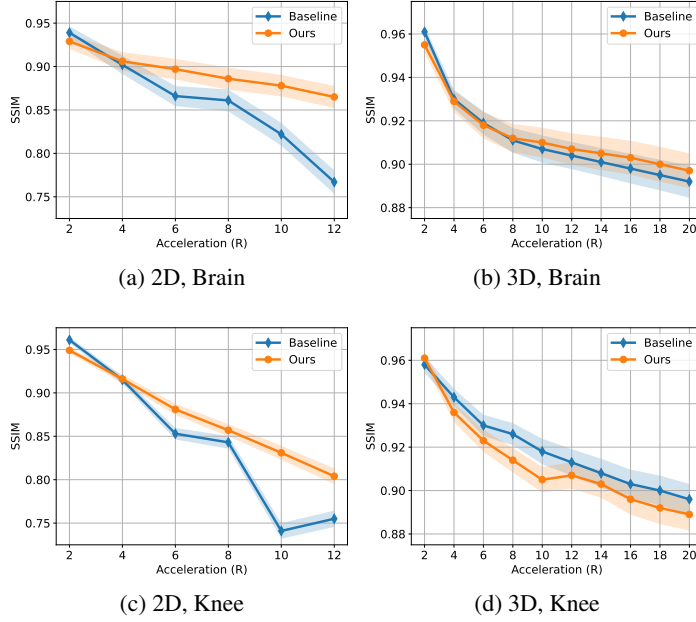


Figure 2: **Mean test SSIM [52] for 2D and 3D patterns on Brains and Knees.** We compare reconstructions with masks learned using our method to those with fixed baseline masks across a range of acceleration factors. The shaded areas indicate a 95% confidence interval. Masks learned with our method consistently lead to better reconstructions than baseline masks for 2D patterns. For 3D patterns, our masks offer competitive performance with baselines.

For the case of Gaussian measurement noise, $\mathbf{y} \sim \mathcal{N}(\mathbf{y}; \mathcal{A}(\mathbf{x}_0), \sigma_{\mathbf{y}}^2 \mathbf{I})$, the approximation in Eq.(8) gives us

$$\nabla_{\mathbf{x}_t} \log p_t(\mathbf{y}|\mathbf{x}_t) \simeq -\frac{1}{\sigma_{\mathbf{y}}^2} \nabla_{\mathbf{x}_t} \|\mathcal{A}(\hat{\mathbf{x}}_0) - \mathbf{y}\|_2^2, \quad (9)$$

where $\hat{\mathbf{x}}_0$ is calculated as in Eq.(7). Finally, using the approximation from Eq.(9), we can sample from the posterior using the reverse SDE from Eq.(5). In practice, calculating the gradient in Eq.(9) requires backpropagating through the score network with respect to the noisy input \mathbf{x}_t .

2.3 MRI Reconstruction

MRI is a popular medical imaging modality due to its superior soft tissue contrast and lack of ionizing radiation. Unfortunately, MRI suffers from long acquisition times. A common approach for accelerating scans is to collect fewer measurements and solve the resulting ill-posed inverse problem. The measurement process for multi-coil MRI can be written in the form

$$\mathbf{y}_i = \mathbf{P} \mathbf{F} \mathbf{S}_i \mathbf{x}_0 + \epsilon, \quad (10)$$

where $\mathbf{y}_i \in \mathbb{C}^m$ are the measurements in the spatial frequency domain (or k -space) for the i^{th} coil, $\mathbf{x}_0 \in \mathbb{C}^n$ is the image of interest, $\mathbf{S}_i \in \mathbb{C}^{n \times n}$ is the coil sensitivity map for the i^{th} coil (c coils in total), $\mathbf{F} \in \mathbb{C}^{n \times n}$ is the Fourier transform matrix, $\mathbf{P} \in \mathbb{C}^{m \times n}$ is a sub-sampling operator whose rows are a subset of the rows of the $n \times n$ identity matrix, and $\epsilon \in \mathbb{C}^m$ is i.i.d Gaussian noise. We also define the *acceleration factor* $R := m/n$ as the under-sampling ratio. Note that even if the number of coils is large and $mc \geq n$ the problem may still be ill-posed as coil sensitivity maps have linear dependence due to spatial correlations.

Many early approaches for MRI reconstruction relied on sparsity-based or low-rank priors [33, 18, 38]. More recently, however, there has been a push to leverage advances in deep learning to assist in under-sampled image reconstruction for MRI. These methods include unrolled techniques [1, 5, 19], as well as approaches leveraging generative models [21, 24, 13, 32].

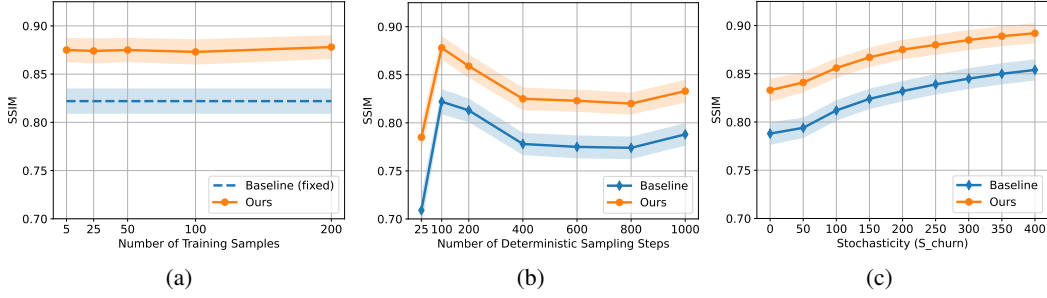


Figure 3: **Test results for varying training and sampling parameters.** We vary (a) the number of training samples for our method, (b) the number of deterministic sampling steps, and (c) the stochasticity of sampling for 1000 steps (determined by S_churn as in Algorithm 1), and present the mean SSIM on the test set. The shaded areas indicate a 95% confidence interval. All experiments are performed on brain scans using 2D patterns with an acceleration of $R=10$.

3 Methods

We would like to learn a distribution $p_{\theta_{\mathcal{A}}}(\mathcal{A})$, parameterized by weights $\theta_{\mathcal{A}}$, over forward operators \mathcal{A} that produce measurements $\mathbf{y} = \mathcal{A}(\mathbf{x}_0) + \epsilon$. Our goal is to minimize the reconstruction error between the true signal \mathbf{x}_0 and the estimates $\tilde{\mathbf{x}}_0 \sim p_0(\mathbf{x}_0|\mathbf{y})$ produced by sampling from the posterior using a diffusion-based generative model. We can write the problem as an optimization that can be solved using gradient descent-based methods:

$$\theta_{\mathcal{A}}^* = \underset{\theta_{\mathcal{A}}}{\operatorname{argmin}} \mathbb{E}_{\mathbf{x}_0 \sim p_0(\mathbf{x}_0), \tilde{\mathbf{x}}_0 \sim p_0(\mathbf{x}_0|\mathbf{y}), \mathbf{y} \sim p(\mathbf{y}|\mathbf{x}_0), \mathcal{A} \sim p_{\theta_{\mathcal{A}}}(\mathcal{A})} \|\mathbf{x}_0 - \tilde{\mathbf{x}}_0\|_2^2. \quad (11)$$

In practice, however, sampling from the posterior to get $\tilde{\mathbf{x}}_0$ involves an iterative application of an SDE solver or ancestral sampling. This makes differentiating with respect to $\theta_{\mathcal{A}}$ challenging, as naively backpropagating through the sampling procedure is infeasible due to memory constraints. In the following sections, we describe our approach to solve this problem.

3.1 Learning Forward Operators

To find a solution, we return to Tweedie’s formula from Section 2.2. For the case of VE SDEs, recall that the noisy signal at time t is given by $p_t(\mathbf{x}_t|\mathbf{x}_0) = \mathcal{N}(\mathbf{x}_t; \mathbf{x}_0, \sigma_t^2 \mathbf{I})$, allowing us to use Eq. (6) to get a one-step approximation of the denoised posterior mean $\mathbb{E}_{\mathbf{x}_t \sim p_t(\mathbf{x}_t|\mathbf{x}_0)}[\mathbf{x}_0|\mathbf{x}_t]$. We show in Proposition 3.1 that we can extend Tweedie’s formula to include measurements $\mathbf{y} \sim p(\mathbf{y}|\mathbf{x}_0)$.

Proposition 3.1 (Tweedie’s formula with additional measurements). *Let $\mathbf{x}_0 \sim p_0(\mathbf{x}_0)$ be an unknown signal, $\mathbf{x}_t \sim p_t(\mathbf{x}_t|\mathbf{x}_0) = \mathcal{N}(\mathbf{x}_t; \mathbf{x}_0, \sigma_t^2 \mathbf{I})$ a version of \mathbf{x}_0 corrupted by additive Gaussian noise, and $\mathbf{y} \sim p(\mathbf{y}|\mathbf{x}_0)$ some additional measurements of \mathbf{x}_0 . Furthermore, let \mathbf{x}_t and \mathbf{y} be conditionally independent given \mathbf{x}_0 : $p_t(\mathbf{x}_t|\mathbf{x}_0, \mathbf{y}) = p_t(\mathbf{x}_t|\mathbf{x}_0)$. Finally, assume that $p_t(\mathbf{x}_t|\mathbf{y})$ is supported everywhere. Then, the posterior mean of \mathbf{x}_0 conditioned on \mathbf{x}_t and \mathbf{y} is given by*

$$\mathbb{E}[\mathbf{x}_0|\mathbf{x}_t, \mathbf{y}] = \mathbf{x}_t + \sigma_t^2 \nabla_{\mathbf{x}_t} \log p_t(\mathbf{x}_t|\mathbf{y}). \quad (12)$$

We give the proof in Appendix A. Recalling that $\nabla_{\mathbf{x}_t} \log p_t(\mathbf{x}_t|\mathbf{y}) = \nabla_{\mathbf{x}_t} \log p_t(\mathbf{x}_t) + \nabla_{\mathbf{x}_t} \log p_t(\mathbf{y}|\mathbf{x}_t)$, our result essentially allows us to leverage the score of the likelihood *in addition* to the prior to obtain a finer estimate of \mathbf{x}_0 than using the prior alone. The assumption of conditional independence of \mathbf{x}_t and \mathbf{y} given \mathbf{x}_0 is satisfied in the inverse problem setting, as we have that $\mathbf{x}_0 \rightarrow \mathbf{y}$ and $\mathbf{x}_0 \rightarrow \mathbf{x}_t$ with no other dependencies.

In reality, we only have access to a score network and a surrogate form of the score of the time-dependent likelihood from Eq. (8). Therefore, a tractable approximation of the expectation in Eq. (12) is

$$\mathbb{E}[\mathbf{x}_0|\mathbf{x}_t, \mathbf{y}] \simeq \mathbf{x}_t + \sigma_t^2 [\mathbf{s}_{\theta}(\mathbf{x}_t, t) + \nabla_{\mathbf{x}_t} \log p_t(\mathbf{y}|\hat{\mathbf{x}}_0)], \quad (13)$$

where $\hat{\mathbf{x}}_0$ is given by Tweedie’s formula as in Eq. (6). In practice, we assume that $p_t(\mathbf{y}|\hat{\mathbf{x}}_0) \sim \mathcal{N}(\mathbf{y}; \mathcal{A}(\hat{\mathbf{x}}_0), \sigma_t^2 \mathbf{I})$ and calculate the posterior mean as

$$\mathbb{E}[\mathbf{x}_0|\mathbf{x}_t, \mathbf{y}] \simeq \mathbf{x}_t + \sigma_t^2 \mathbf{s}_{\theta}(\mathbf{x}_t, t) - \gamma \nabla_{\mathbf{x}_t} \|\mathcal{A}(\hat{\mathbf{x}}_0) - \mathbf{y}\|_2^2, \quad (14)$$

where γ is a likelihood step size.

Using the result from Proposition 3.1, we finally present our training objective:

$$\begin{aligned} \theta_{\mathcal{A}}^* &= \underset{\theta_{\mathcal{A}}}{\operatorname{argmin}} \mathbb{E}_{\mathbf{x}_0 \sim p_0(\mathbf{x}_0)} \|\mathbf{x}_0 - \tilde{\mathbf{x}}_0\|_2^2 \\ \tilde{\mathbf{x}}_0 &= \mathbb{E}_{\mathcal{A} \sim p_{\theta_{\mathcal{A}}}(A), \mathbf{y} \sim \mathcal{N}(A(\mathbf{x}_0), \sigma_{\mathbf{y}}^2 \mathbf{I}), \mathbf{x}_t \sim p_t(\mathbf{x}_t | \mathbf{x}_0), t \sim q_t(t)} [\mathbf{x}_0 | \mathbf{x}_t, \mathbf{y}], \end{aligned} \quad (15)$$

where $q_t(t)$ is a distribution over time steps and we use the approximation from Eq. (14) to calculate the posterior mean estimate $\tilde{\mathbf{x}}_0$. During training, we calculate the gradient w.r.t $\theta_{\mathcal{A}}$ with automatic differentiation (e.g. using PyTorch [35]), which involves backpropagating through $\tilde{\mathbf{x}}_0$ and therefore through the score network.

Starting with a noisy signal at time t , samplers for diffusion models generally follow the approach of: get the denoised estimate $\hat{\mathbf{x}}_0$ at time t using the score network, then add back the appropriate amount of noise for time $t - 1$ and repeat. Therefore, by learning forward operators that produce good one-step posterior denoised estimates, our method facilitates good final reconstructions. We are able to use powerful generative models “off-the-shelf” without further training. Furthermore, since we decouple our training objective from the posterior sampling scheme, forward operators learned with our method are flexible and agnostic to the choice of sampler.

3.2 Parameterizing the Sampling Pattern

We wish to learn a distribution over optimal sampling pattern for reconstructing MRI images for some fixed acceleration R . This amounts to learning $\mathcal{A}_i(\mathbf{x}) = \mathbf{PFS}_i\mathbf{x}$, for $i \in [c]$ with \mathbf{F} and \mathbf{S}_i fixed. Therefore, we only need to learn a distribution $p_{\theta_{\mathbf{P}}}$ parameterized by weights $\theta_{\mathbf{P}}$ over the sub-sampling operator \mathbf{P} . We base our parameterization and sampling scheme on that of LOUPE [55], with some changes. For n -dimensional images, we learn parameters $\theta_{\mathbf{P}} \in \mathbb{R}^n$. Each entry $\theta_{\mathbf{P},i}$, $i \in [n]$, defines an independent Bernouli random variable $\mathcal{B}(p(\theta_{\mathbf{P},i}))$ at each location in the k-space of an image, where $p(\theta_{\mathbf{P},i})$ is the probability that the variable takes the value 1. The sampling mask distribution is defined as $p_{\theta_{\mathbf{P}}} = \prod_{i=1}^n \mathcal{B}(p(\theta_{\mathbf{P},i}))$.

Following LOUPE, we re-scale the values $\sigma(\theta_{\mathbf{P},i})$, where $\sigma(x) = 1/(1 + e^{-x})$ is the standard sigmoid function, so that they have mean $1/R$. Since the Bernouli random variables are independent, sample patterns drawn from the re-scaled distribution will have an average acceleration factor of R . Given the unnormalized mean $\bar{p} = \frac{1}{n} \sum_{i=1}^n \sigma(\theta_{\mathbf{P},i})$, we define $p(\theta_{\mathbf{P},i})$ as

$$p(\theta_{\mathbf{P},i}) = \begin{cases} \frac{1}{\bar{p}R} \sigma(\theta_{\mathbf{P},i}) & \text{if } \bar{p} \geq \frac{1}{R} \\ 1 - \frac{R-1}{R-\bar{p}R} (1 - \sigma(\theta_{\mathbf{P},i})) & \text{otherwise} \end{cases}, \quad (16)$$

which outputs values in the range $[0, 1]$ and has the desired mean $\frac{1}{n} \sum_{i=1}^n p(\theta_{\mathbf{P},i}) = 1/R$.

Next, we need to sample from $p_{\theta_{\mathbf{P}}}$ in a way that is differentiable with respect to $\theta_{\mathbf{P}}$. We use the Gumbel Straight-Through estimator [26], which shows superior performance to the vanilla Straight-Through estimator [8] used by LOUPE. For samples g_1 and g_2 drawn i.i.d. from the Gumbel(0, 1) distribution and temperature $\tau > 0$, the Gumbel Straight-Through estimator generates a sample $z_i \in \{0, 1\}$ for k-space location $i \in [n]$ as

$$z_i = \mathbf{1}_{\geq 0.5}(y_i), \quad y_i = \frac{u_{\tau}(p(\theta_{\mathbf{P},i}), g_1)}{u_{\tau}(p(\theta_{\mathbf{P},i}), g_1) + u_{\tau}(1 - p(\theta_{\mathbf{P},i}), g_2)}, \quad u_{\tau}(p, g) = \exp\left(\frac{\log p + g}{\tau}\right), \quad (17)$$

where $\mathbf{1}_{\geq 0.5}(\cdot)$ is the indicator function that takes the value 1 if its argument is ≥ 0.5 and 0 otherwise. As $\tau \rightarrow 0$, we have that $\mathbb{E}[y_i] \rightarrow p(\theta_{\mathbf{P},i})$. The Gumbel Straight-Through estimator replaces $\nabla_{\theta_{\mathbf{P}}} z_i$ with $\nabla_{\theta_{\mathbf{P}}} y_i$ during backpropagation. This trick allows us to draw realistic binary samples z_i while enjoying well-defined gradients from the smooth softmax sample y_i .

Algorithm 1 Posterior sampling

Require: $\mathbf{s}_{\theta}(\mathbf{x}_t, t)$, $\sigma_{t \in \{t_N, \dots, t_0\}}$, S_{churn} , ρ_{dps} , \mathbf{y}

- 1: **sample** $\mathbf{x}_N \sim \mathcal{N}(\mathbf{0}, \sigma_{t_N}^2 \mathbf{I})$
- 2: **for** $i \in \{N, \dots, 1\}$ **do**
- 3: **sample** $\mathbf{z}_i \sim \mathcal{N}(\mathbf{0}, \mathbf{I})$
- 4: $\alpha_i \leftarrow \min(S_{\text{churn}}/N, \sqrt{2} - 1)$
- 5: $\hat{\sigma}_{t_i} \leftarrow \sigma_{t_i} + \alpha_i \sigma_{t_i}$
- 6: $\hat{\mathbf{x}}_i \leftarrow \mathbf{x}_i + \sqrt{\hat{\sigma}_{t_i}^2 - \sigma_{t_i}^2} \mathbf{z}_i$
- 7: $\hat{\mathbf{x}}_0 \leftarrow \hat{\mathbf{x}}_i + \hat{\sigma}_{t_i}^2 \mathbf{s}_{\theta}(\hat{\mathbf{x}}_i, \hat{t}_i)$
- 8: $\hat{\mathbf{x}}'_i \leftarrow \hat{\mathbf{x}}_i + (\hat{\sigma}_{t_i} - \sigma_{t_{i-1}}) \mathbf{s}_{\theta}(\hat{\mathbf{x}}_i, \hat{t}_i)$
- 9: $\mathbf{x}_{i-1} \leftarrow \hat{\mathbf{x}}'_i - \rho_{\text{dps}} \nabla_{\hat{\mathbf{x}}_i} \|\mathcal{A}(\hat{\mathbf{x}}_0) - \mathbf{y}\|_2^2$
- 10: **return** \mathbf{x}_0

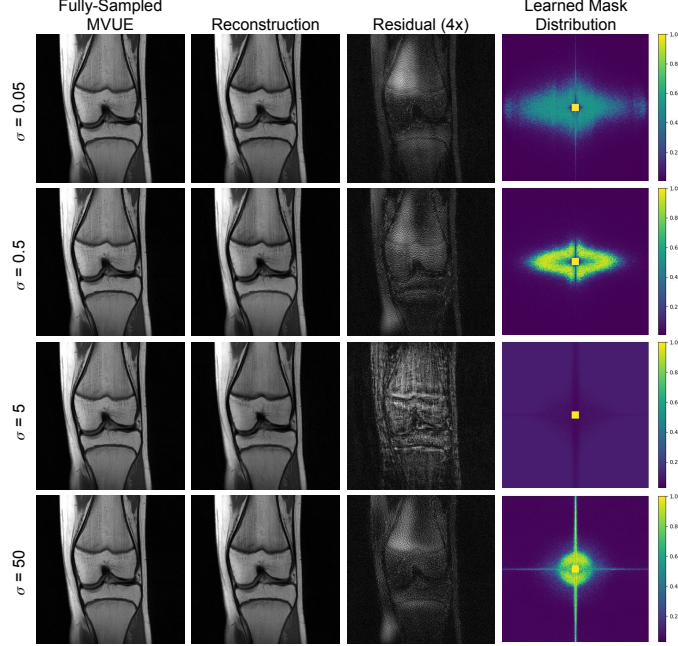


Figure 4: **Learned masks and reconstructions for fixed noise level during training.** We fix the value of σ during training instead of sampling it randomly to investigate the effects of noise level on learning. Very low ($\sigma = 0.05, 0.5$) and very high ($\sigma = 50$) noise levels lead to useful masks while moderate levels ($\sigma = 5$) do not converge. We colorize the learned probability distribution and scale the residual images by a factor of 4 for easier viewing. All patterns are 3D with $R = 10$

4 Experiments

We experiment on the fastMRI multi-coil brain and knee datasets [54]. We create single-coil minimum variance unbiased estimator (MVUE) images from the fully-sampled k-space data and sensitivity maps (calculated using ESPIRiT [46]) to use as our ground truth reference. For training and testing sub-sampling patterns, we create a subset of 200 training and 50 validation scans from the fastMRI training set and 100 test scans from the fastMRI validation set. We perform retrospective sub-sampling in our sampling pattern experiments, meaning that we artificially apply sampling masks to fully-sampled k-space data.

We train score-based networks using the ADM architecture [14] with the EDM repo [27]. We use the EDM [27] default pre-conditioning and training parameters, with a learning rate of 1×10^{-4} , batch size of 15, and an exponential moving average (ema) half-life of 100K images, and train the models for 140 epochs. For posterior sampling, we modify the the stochastic sampling algorithm from EDM to have no second-order correction and add a log-likelihood step. We present our posterior sampler in Algorithm 1. Following the implementation of DPS [12], we set the sampling likelihood step size parameter as $\rho_{dps} = \rho / \|\mathbf{y} - \mathcal{A}(\hat{\mathbf{x}}_0)\|$, where ρ is a tuneable hyperparameter. Unless otherwise stated, we use 100 sampling steps with $\rho = 10$ and the stochasticity parameter $S_{churn} = 0$.

When learning sub-sampling patterns, we use the noise schedule from EDM with $\sigma_t = t$ and noise distribution $q_t(t) = q_{\sigma_t}(\sigma_t)$ such that $\ln \sigma_t \sim \mathcal{N}(P_{mean}, P_{std}^2)$, where we use the default values $P_{mean} = -1.2$ and $P_{std} = 1.2$ [27]. We set the measurement noise $\sigma_y = 0$, training likelihood step size to $\gamma = 1$, training batch size to 1, and Gumbel temperature to $\tau = 1$. We use the Adam optimizer [29] with a learning rate of 1×10^{-2} and optimize for 10 epochs over all 200 training samples, unless stated otherwise. We fix a central 16-pixel wide region that is always fully sampled for calibration purposes on both our masks and baselines, and initialize pattern weights as $\theta_P = \mathbf{0}$. We perform all experiments on a machine with $4 \times$ Nvidia A100 GPUs.

4.1 Comparison to Baseline Patterns

First, we train 2D and 3D sub-sampling pattern distributions for brain and knee scans across various accelerations. As a baseline, we compare to posterior sampling reconstructions using fixed equispaced masks for the 2D case and Poisson disc masks for 3D. We display qualitative results in Figure 1. Our masks can reduce small- and large-scale artifacts compared to baseline masks, as shown by the areas indicated with red arrows and insets in Figure 1. We note that our brain reconstruction at $R = 20$ displays a shading artifact in the top-left region, and both the baseline and our knee reconstructions display shading artifacts. While our method displays good performance, reconstructions still show limited quality for 2D patterns and high accelerations regardless of training.

We evaluate the performance of each method using the structural similarity index measure (SSIM) [52] between the reference MVUE and the reconstruction and plot the results in Figure 2. Our method achieves better reconstruction error for 2D imaging in both anatomies at acceleration values $R > 4$, as indicated in Figure 2(a) and (c). Interestingly Figures 2(b) and (d) show that both our masks and the Poisson disc masks perform similarly in the 3D case, with the only significant difference being that our masks lead to slightly worse SSIM for knee scans for $R = 8$ and $R = 10$. We note that training a diffusion model end-to-end or fine-tuning a pre-trained model with the objective in Eq. (15) may offer better performance. However, these approaches would be more computationally expensive and couple the diffusion model with the forward operator, decreasing generalization ability and reducing the usefulness of the generator for other tasks.

4.2 Varying Parameters

Here, we test how changing various training and sampling parameters changes the quality of reconstructions. We fix the test set to brain scans and evaluate 2D patterns with $R = 10$ to easily compare results between the experiments. We show the results in Figure 3.

First, we vary the number of training samples for our method. We train sampling patterns for a total of 2000 iterations with a batch size of 1 regardless of the number of samples (e.g. for 5 samples we train for 400 epochs and for 25 samples we train for 80 epochs) and evaluate on the same 100 test images. The results in Figure 3(a) show that our method learns a pattern that can outperform a fixed, equispaced baseline with as few as five samples. Next, we vary the number of deterministic sampling steps, keeping the learned sampling pattern distribution fixed. As shown in Figure 3(b), the relative performance between the two methods remains invariant to changing number of steps. Third, we introduce randomness into sampling by varying S_{churn} , fixing the number of sampling steps to 1000 and changing ρ to 2. Figure 3 indicates that the relative performance between our masks and the equispaced masks does not change. The modularity of our method allows us to train sampling operators that are uncoupled from the sampler choice at inference time.

4.3 Effects of Noise Level on Training

In this experiment, we fix the anatomy to knees and the pattern to 3D with $R = 10$. During training, instead of drawing the noise level σ_t randomly, we fix it to a single value σ . We show the visual reconstruction results in Figure 4. At lower noise levels ($\sigma = 0.05, 0.5$), the patterns capture more high-frequency portions of k-space, while at the highest noise level ($\sigma = 50$) the pattern densely sampled the central region of k-space. Intuitively, lower levels of additive noise during training means that the score network can more accurately predict the denoised image, with the measurements aiding by adding fine details to the blurry denoised image. For $\sigma = 50$, the signal-to-noise ratio is almost zero, so the posterior mean estimate relies heavily on the measurements to provide low-frequency information. We note that the pattern for $\sigma = 5$ did not converge to a useful mask. This indicates that there may be a “dead zone” of poor values for σ during training.

5 Limitations and Broader Impact

Limitations. The main limitation of our method is that it has a high memory complexity. Our training objective requires backpropagating through the posterior mean estimate, which itself relies on backpropagating through the score network to obtain the approximation of the log-likelihood gradient. This process calculates and stores second-order derivatives, which are very large for high-dimensional problems. Another limitation is that we only consider Cartesian sampling patterns, while

non-Cartesian patterns may offer improved reconstruction quality and robustness to patient motion during scanning. We emphasize that our work focuses on the novel methodology and additional clinical evaluation would be needed before it can be usable for MR protocol designs.

Broader Impact. Learning sampling patterns that offer the same reconstruction quality as variable density or fixed patterns at higher accelerations would allow patients to be scanned in a shorter time. This would benefit patients by decreasing costs. However, a potential negative impact of our method is that the training data may bias the sampling patterns toward a certain demographic. For example, if the training data are all from patients under the age of 20, the learned sampling patterns may offer poor reconstruction quality for older patients. Care must be taken to construct the training and evaluation sets to mitigate any such bias.

6 Conclusion

We introduced a method to learn sub-sampling operators for reconstructing MRI images using posterior sampling with a diffusion-based generative model. We rely on an extension of Tweedie’s formula for inverse problems, using pre-trained generators with no need for re-training. Further, our method is agnostic to the choice of sampling scheme at inference time. Experiments demonstrate better performance than equispaced masks for 2D imaging and similar performance to Poisson Discs for 3D imaging. Our method can learn competitive patterns with as few as five training samples.

References

- [1] Hemant K Aggarwal, Merry P Mani, and Mathews Jacob. Modl: Model-based deep learning architecture for inverse problems. *IEEE transactions on medical imaging*, 38(2):394–405, 2018.
- [2] Hemant Kumar Aggarwal and Mathews Jacob. J-MoDL: Joint model-based deep learning for optimized sampling and reconstruction. *IEEE Journal of Selected Topics in Signal Processing*, 14(6):1151–1162, oct 2020.
- [3] Cagan Alkan, Morteza Mardani, Shreyas Vasanawala, and John M. Pauly. Learning to sample MRI via variational information maximization. In *NeurIPS 2020 Workshop on Deep Learning and Inverse Problems*, 2020.
- [4] Brian D.O. Anderson. Reverse-time diffusion equation models. *Stochastic Processes and their Applications*, 12(3):313–326, 1982.
- [5] Marius Arvinte, Sriram Vishwanath, Ahmed H. Tewfik, and Jonathan I. Tamir. Deep j-sense: Accelerated mri reconstruction via unrolled alternating optimization, 2021.
- [6] Muhammad Asim, Ali Ahmed, and Paul Hand. Invertible generative models for inverse problems: mitigating representation error and dataset bias. *ArXiv*, abs/1905.11672, 2020.
- [7] Cagla D. Bahadir, Alan Q. Wang, Adrian V. Dalca, and Mert R. Sabuncu. Deep-learning-based optimization of the under-sampling pattern in mri. 2019.
- [8] Yoshua Bengio, Nicholas Léonard, and Aaron C. Courville. Estimating or propagating gradients through stochastic neurons for conditional computation. *ArXiv*, abs/1308.3432, 2013.
- [9] Ashish Bora, Ajil Jalal, Eric Price, and Alexandros G. Dimakis. Compressed sensing using generative models. In *ICML*, 2017.
- [10] Ashish Bora, Eric Price, and Alexandros G. Dimakis. AmbientGAN: Generative models from lossy measurements. In *International Conference on Learning Representations*, 2018.
- [11] Emmanuel J. Candès, Justin K. Romberg, and Terence Tao. Stable signal recovery from incomplete and inaccurate measurements. *Communications on Pure and Applied Mathematics*, 59:1207–1223, 2005.
- [12] Hyungjin Chung, Jeongsol Kim, Michael Thompson Mccann, Marc Louis Klasky, and Jong Chul Ye. Diffusion posterior sampling for general noisy inverse problems. In *The Eleventh International Conference on Learning Representations*, 2023.
- [13] Hyungjin Chung and Jong Chul Ye. Score-based diffusion models for accelerated mri. *Medical Image Analysis*, 80:102479, 2022.

- [14] Prafulla Dhariwal and Alexander Nichol. Diffusion models beat gans on image synthesis. *Advances in Neural Information Processing Systems*, 34:8780–8794, 2021.
- [15] D.L. Donoho. Compressed sensing. *IEEE Transactions on Information Theory*, 52(4):1289–1306, 2006.
- [16] Bradley Efron. Tweedie’s formula and selection bias. *Journal of the American Statistical Association*, 106:1602–1614, 12 2011.
- [17] Mark A Griswold, Peter M Jakob, Robin M Heidemann, Mathias Nittka, Vladimir Jellus, Jianmin Wang, Berthold Kiefer, and Axel Haase. Generalized autocalibrating partially parallel acquisitions (grappa). *Magnetic Resonance in Medicine: An Official Journal of the International Society for Magnetic Resonance in Medicine*, 47(6):1202–1210, 2002.
- [18] Justin P. Haldar and Kavin Setsompop. Linear predictability in magnetic resonance imaging reconstruction: Leveraging shift-invariant fourier structure for faster and better imaging. *IEEE Signal Processing Magazine*, 37(1):69–82, 2020.
- [19] Kerstin Hammernik, Teresa Klatzer, Erich Kobler, Michael P. Recht, Daniel K. Sodickson, Thomas Pock, and Florian Knoll. Learning a variational network for reconstruction of accelerated mri data. *Magnetic Resonance in Medicine*, 79(6):3055–3071, 2018.
- [20] Paul Hand, Oscar Leong, and Vlad Voroninski. Phase retrieval under a generative prior. In S. Bengio, H. Wallach, H. Larochelle, K. Grauman, N. Cesa-Bianchi, and R. Garnett, editors, *Advances in Neural Information Processing Systems*, volume 31. Curran Associates, Inc., 2018.
- [21] Reinhard Heckel and Paul Hand. Deep decoder: Concise image representations from untrained non-convolutional networks. *ArXiv*, abs/1810.03982, 2019.
- [22] Jonathan Ho, Ajay Jain, and Pieter Abbeel. Denoising diffusion probabilistic models. *Advances in Neural Information Processing Systems*, 33:6840–6851, 2020.
- [23] Jonathan Ho and Tim Salimans. Classifier-free diffusion guidance. *arXiv preprint arXiv:2207.12598*, 2022.
- [24] Ajil Jalal, Marius Arvinte, Giannis Daras, Eric Price, Alexandros G Dimakis, and Jon Tamir. Robust compressed sensing mri with deep generative priors. In M. Ranzato, A. Beygelzimer, Y. Dauphin, P.S. Liang, and J. Wortman Vaughan, editors, *Advances in Neural Information Processing Systems*, volume 34, pages 14938–14954. Curran Associates, Inc., 2021.
- [25] Ajil Jalal, Sushrut Karmalkar, Alexandros G. Dimakis, and Eric Price. Instance-optimal compressed sensing via posterior sampling, 2021.
- [26] Eric Jang, Shixiang Gu, and Ben Poole. Categorical reparameterization with gumbel-softmax. In *International Conference on Learning Representations*, 2017.
- [27] Tero Karras, Miika Aittala, Timo Aila, and Samuli Laine. Elucidating the design space of diffusion-based generative models. In *Proc. NeurIPS*, 2022.
- [28] Bahjat Kwar, Michael Elad, Stefano Ermon, and Jiaming Song. Denoising diffusion restoration models. *arXiv preprint arXiv:2201.11793*, 2022.
- [29] Diederik P. Kingma and Jimmy Ba. Adam: A method for stochastic optimization. In Yoshua Bengio and Yann LeCun, editors, *3rd International Conference on Learning Representations, ICLR 2015, San Diego, CA, USA, May 7-9, 2015, Conference Track Proceedings*, 2015.
- [30] Carole Lazarus, Pierre Weiss, Nicolas Chauffert, Franck Mauconduit, Loubna El Gueddari, Christophe Destrieux, Ilyess Zemmoura, Alexandre Vignaud, and Philippe Ciuciu. Sparkling: variable-density k-space filling curves for accelerated t2*-weighted mri. *Magnetic Resonance in Medicine*, 81(6):3643–3661, 2019.
- [31] Zhaoqiang Liu, Selwyn Gomes, Avtansh Tiwari, and Jonathan Scarlett. Sample complexity bounds for 1-bit compressive sensing and binary stable embeddings with generative priors, 2020.
- [32] Guanxiong Luo, Martin Heide, and Martin Uecker. Mri reconstruction via data driven markov chain with joint uncertainty estimation. *arXiv preprint arXiv:2202.01479*, 2022.
- [33] Michael Lustig, David Donoho, and John M Pauly. Sparse mri: The application of compressed sensing for rapid mr imaging. *Magnetic Resonance in Medicine: An Official Journal of the International Society for Magnetic Resonance in Medicine*, 58(6):1182–1195, 2007.

- [34] Gregory Ongie, Ajil Jalal, Christopher A Metzler, Richard G Baraniuk, Alexandros G Dimakis, and Rebecca Willett. Deep learning techniques for inverse problems in imaging. *IEEE Journal on Selected Areas in Information Theory*, 1(1):39–56, 2020.
- [35] Adam Paszke, Sam Gross, Soumith Chintala, Gregory Chanan, Edward Yang, Zachary DeVito, Zeming Lin, Alban Desmaison, Luca Antiga, and Adam Lerer. Automatic differentiation in pytorch. 2017.
- [36] Klaas P Pruessmann, Markus Weiger, Markus B Scheidegger, and Peter Boesiger. Sense: sensitivity encoding for fast mri. *Magnetic Resonance in Medicine: An Official Journal of the International Society for Magnetic Resonance in Medicine*, 42(5):952–962, 1999.
- [37] Shuang Qiu, Xiaohan Wei, and Zhuoran Yang. Robust one-bit recovery via relu generative networks: Improved statistical rates and global landscape analysis. *arXiv preprint arXiv:1908.05368*, 2019.
- [38] Saiprasad Ravishankar and Yoram Bresler. Mr image reconstruction from highly undersampled k-space data by dictionary learning. *IEEE Transactions on Medical Imaging*, 30(5):1028–1041, 2011.
- [39] Ferdia Sherry, Martin Benning, Juan Carlos De los Reyes, Martin J Graves, Georg Maierhofer, Guy Williams, Carola-Bibiane Schönlieb, and Matthias J Ehrhardt. Learning the sampling pattern for mri. *IEEE Transactions on Medical Imaging*, 39(12):4310–4321, 2020.
- [40] Daniel K Sodickson and Warren J Manning. Simultaneous acquisition of spatial harmonics (smash): fast imaging with radiofrequency coil arrays. *Magnetic resonance in medicine*, 38(4):591–603, 1997.
- [41] Yang Song and Stefano Ermon. Generative modeling by estimating gradients of the data distribution. *Advances in neural information processing systems*, 32, 2019.
- [42] Yang Song and Stefano Ermon. Improved techniques for training score-based generative models. *arXiv preprint arXiv:2006.09011*, 2020.
- [43] Yang Song, Liyue Shen, Lei Xing, and Stefano Ermon. Solving inverse problems in medical imaging with score-based generative models. In *International Conference on Learning Representations*, 2022.
- [44] Yang Song, Jascha Sohl-Dickstein, Diederik P Kingma, Abhishek Kumar, Stefano Ermon, and Ben Poole. Score-based generative modeling through stochastic differential equations. In *International Conference on Learning Representations*, 2021.
- [45] Anuroop Sriram, Jure Zbontar, Tullie Murrell, Aaron Defazio, C Lawrence Zitnick, Nafissa Yakubova, Florian Knoll, and Patricia Johnson. End-to-end variational networks for accelerated mri reconstruction. In *Medical Image Computing and Computer Assisted Intervention–MICCAI 2020: 23rd International Conference, Lima, Peru, October 4–8, 2020, Proceedings, Part II 23*, pages 64–73. Springer, 2020.
- [46] Martin Uecker, Peng Lai, Mark J Murphy, Patrick Virtue, Michael Elad, John M Pauly, Shreyas S Vasanawala, and Michael Lustig. Espirit—an eigenvalue approach to autocalibrating parallel mri: where sense meets grappa. *Magnetic resonance in medicine*, 71(3):990–1001, 2014.
- [47] Dmitry Ulyanov, Andrea Vedaldi, and Victor S. Lempitsky. Deep image prior. *2018 IEEE/CVF Conference on Computer Vision and Pattern Recognition*, pages 9446–9454, 2018.
- [48] Pascal Vincent. A connection between score matching and denoising autoencoders. *Neural computation*, 23(7):1661–1674, 2011.
- [49] Guanhua Wang, Tianrui Luo, Jon-Fredrik Nielsen, Douglas C Noll, and Jeffrey A Fessler. B-spline parameterized joint optimization of reconstruction and k-space trajectories (bjork) for accelerated 2d mri. *IEEE Transactions on Medical Imaging*, 41(9):2318–2330, 2022.
- [50] Guanhua Wang, Jon-Fredrik Nielsen, Jeffrey A. Fessler, and Douglas C. Noll. Stochastic optimization of 3d non-cartesian sampling trajectory (snopy), 2022.
- [51] Guanhua Wang, Douglas C. Noll, and Jeffrey A. Fessler. Adaptive sampling for linear sensing systems via langevin dynamics, 2023.
- [52] Zhou Wang, A.C. Bovik, H.R. Sheikh, and E.P. Simoncelli. Image quality assessment: from error visibility to structural similarity. *IEEE Transactions on Image Processing*, 13(4):600–612, 2004.

- [53] Jay Whang, Mauricio Delbracio, Hossein Talebi, Chitwan Saharia, Alexandros G Dimakis, and Peyman Milanfar. Deblurring via stochastic refinement. *arXiv preprint arXiv:2112.02475*, 2021.
- [54] Jure Zbontar, Florian Knoll, Anuroop Sriram, Tullie Murrell, Zhengnan Huang, Matthew J Muckley, Aaron Defazio, Ruben Stern, Patricia Johnson, Mary Bruno, et al. fastmri: An open dataset and benchmarks for accelerated mri. *arXiv preprint arXiv:1811.08839*, 2018.
- [55] Jinwei Zhang, Hang Zhang, Alan Wang, Qihao Zhang, Mert Sabuncu, Pascal Spincemaille, Thanh D. Nguyen, and Yi Wang. Extending loupe for k-space under-sampling pattern optimization in multi-coil mri, 2020.
- [56] Marcelo VW Zibetti, Gabor T Herman, and Ravinder R Regatte. Fast data-driven learning of parallel mri sampling patterns for large scale problems. *Scientific Reports*, 11(1):19312, 2021.

A Proof of Proposition 3.1

Proposition 3.1 (Tweedie’s formula with additional measurements). *Let $\mathbf{x}_0 \sim p_0(\mathbf{x}_0)$ be an unknown signal, $\mathbf{x}_t \sim p_t(\mathbf{x}_t|\mathbf{x}_0) = \mathcal{N}(\mathbf{x}_t; \mathbf{x}_0, \sigma_t^2 \mathbf{I})$ a version of \mathbf{x}_0 corrupted by additive Gaussian noise, and $\mathbf{y} \sim p(\mathbf{y}|\mathbf{x}_0)$ some additional measurements of \mathbf{x}_0 . Furthermore, let \mathbf{x}_t and \mathbf{y} be conditionally independent given \mathbf{x}_0 : $p_t(\mathbf{x}_t|\mathbf{x}_0, \mathbf{y}) = p_t(\mathbf{x}_t|\mathbf{x}_0)$. Finally, assume that $p_t(\mathbf{x}_t|\mathbf{y})$ is supported everywhere. Then, the posterior mean of \mathbf{x}_0 conditioned on \mathbf{x}_t and \mathbf{y} is given by*

$$\mathbb{E}[\mathbf{x}_0|\mathbf{x}_t, \mathbf{y}] = \mathbf{x}_t + \sigma_t^2 \nabla_{\mathbf{x}_t} \log p_t(\mathbf{x}_t|\mathbf{y}). \quad (12)$$

Proof. We begin by representing the distribution $p_t(\mathbf{x}_t|\mathbf{y})$ as marginalizing out \mathbf{x}_0 conditioned on \mathbf{y} :

$$p_t(\mathbf{x}_t|\mathbf{y}) = \int_{\mathbf{x}_0} p_t(\mathbf{x}_t|\mathbf{x}_0, \mathbf{y}) p_0(\mathbf{x}_0|\mathbf{y}) d\mathbf{x}_0.$$

Next, we take the gradient w.r.t. \mathbf{x}_t on both sides:

$$\begin{aligned} \nabla_{\mathbf{x}_t} p_t(\mathbf{x}_t|\mathbf{y}) &= \nabla_{\mathbf{x}_t} \int_{\mathbf{x}_0} p_t(\mathbf{x}_t|\mathbf{x}_0, \mathbf{y}) p_0(\mathbf{x}_0|\mathbf{y}) d\mathbf{x}_0 \\ &= \int_{\mathbf{x}_0} p_0(\mathbf{x}_0|\mathbf{y}) \nabla_{\mathbf{x}_t} p_t(\mathbf{x}_t|\mathbf{x}_0, \mathbf{y}) d\mathbf{x}_0 \\ &= \int_{\mathbf{x}_0} p_0(\mathbf{x}_0|\mathbf{y}) p_t(\mathbf{x}_t|\mathbf{x}_0, \mathbf{y}) \nabla_{\mathbf{x}_t} \log p_t(\mathbf{x}_t|\mathbf{x}_0, \mathbf{y}) d\mathbf{x}_0. \end{aligned}$$

On the last line, we use the identity $\nabla_x \log f(x) = \nabla_x f(x)/f(x)$. We note that since $p_t(\mathbf{x}_t|\mathbf{x}_0, \mathbf{y}) = p_t(\mathbf{x}_t|\mathbf{x}_0)$, and $p_t(\mathbf{x}_t|\mathbf{x}_0)$ is Gaussian, $p_t(\mathbf{x}_t|\mathbf{x}_0, \mathbf{y})$ has non-zero value everywhere and we avoid singularities from the denominator.

Continuing, we use the conditional independence of \mathbf{x}_t and \mathbf{y} given \mathbf{x}_0 to replace $\nabla_{\mathbf{x}_t} \log p_t(\mathbf{x}_t|\mathbf{x}_0, \mathbf{y})$ on the right-hand side with $\nabla_{\mathbf{x}_t} \log p_t(\mathbf{x}_t|\mathbf{x}_0)$ and obtain:

$$\begin{aligned} \nabla_{\mathbf{x}_t} p_t(\mathbf{x}_t|\mathbf{y}) &= \int_{\mathbf{x}_0} p_0(\mathbf{x}_0|\mathbf{y}) p_t(\mathbf{x}_t|\mathbf{x}_0, \mathbf{y}) \nabla_{\mathbf{x}_t} \log p_t(\mathbf{x}_t|\mathbf{x}_0) d\mathbf{x}_0 \\ &= \int_{\mathbf{x}_0} p_0(\mathbf{x}_0|\mathbf{y}) p_t(\mathbf{x}_t|\mathbf{x}_0, \mathbf{y}) \left(\frac{\mathbf{x}_0 - \mathbf{x}_t}{\sigma_t^2} \right) d\mathbf{x}_0. \end{aligned}$$

Here, we use the fact that $p_t(\mathbf{x}_t|\mathbf{x}_0) = \mathcal{N}(\mathbf{x}_t; \mathbf{x}_0, \sigma_t^2 \mathbf{I}_n)$ is a Gaussian and replace the score function $\nabla_{\mathbf{x}_t} \log p_t(\mathbf{x}_t|\mathbf{x}_0)$ by its exact value, $(\mathbf{x}_0 - \mathbf{x}_t)/\sigma_t^2$.

Expanding the right-hand-side, we get:

$$\begin{aligned} \nabla_{\mathbf{x}_t} p_t(\mathbf{x}_t|\mathbf{y}) &= \frac{1}{\sigma_t^2} \left[\int_{\mathbf{x}_0} p_0(\mathbf{x}_0|\mathbf{y}) p_t(\mathbf{x}_t|\mathbf{x}_0, \mathbf{y}) \mathbf{x}_0 d\mathbf{x}_0 - \int_{\mathbf{x}_0} p_0(\mathbf{x}_0|\mathbf{y}) p_t(\mathbf{x}_t|\mathbf{x}_0, \mathbf{y}) \mathbf{x}_t d\mathbf{x}_0 \right] \\ &= \frac{1}{\sigma_t^2} \left[\int_{\mathbf{x}_0} p_0(\mathbf{x}_0|\mathbf{y}) p_t(\mathbf{x}_t|\mathbf{x}_0, \mathbf{y}) \mathbf{x}_0 d\mathbf{x}_0 - \mathbf{x}_t \int_{\mathbf{x}_0} p_0(\mathbf{x}_0|\mathbf{y}) p_t(\mathbf{x}_t|\mathbf{x}_0, \mathbf{y}) d\mathbf{x}_0 \right] \\ &= \frac{1}{\sigma_t^2} \left[\int_{\mathbf{x}_0} p_0(\mathbf{x}_0|\mathbf{y}) p_t(\mathbf{x}_t|\mathbf{x}_0, \mathbf{y}) \mathbf{x}_0 d\mathbf{x}_0 - \mathbf{x}_t p_t(\mathbf{x}_t|\mathbf{y}) \right]. \end{aligned}$$

In the previous line, we marginalize out \mathbf{x}_0 conditioned on \mathbf{y} as in the first line of the proof to recover $p_t(\mathbf{x}_t|\mathbf{y})$.

Next, we observe that Bayes’ rule tells us $p_0(\mathbf{x}_0|\mathbf{y}) p_t(\mathbf{x}_t|\mathbf{x}_0, \mathbf{y}) = p_t(\mathbf{x}_t|\mathbf{y}) p_0(\mathbf{x}_0|\mathbf{x}_t, \mathbf{y})$ and replace the former quantity by the latter on the right-hand side:

$$\begin{aligned} \nabla_{\mathbf{x}_t} p_t(\mathbf{x}_t|\mathbf{y}) &= \frac{1}{\sigma_t^2} \left[\int_{\mathbf{x}_0} p_t(\mathbf{x}_t|\mathbf{y}) p_0(\mathbf{x}_0|\mathbf{x}_t, \mathbf{y}) \mathbf{x}_0 d\mathbf{x}_0 - \mathbf{x}_t p_t(\mathbf{x}_t|\mathbf{y}) \right] \\ &= \frac{1}{\sigma_t^2} \left[p_t(\mathbf{x}_t|\mathbf{y}) \mathbb{E}[\mathbf{x}_0|\mathbf{x}_t, \mathbf{y}] - \mathbf{x}_t p_t(\mathbf{x}_t|\mathbf{y}) \right] \\ &= \frac{p_t(\mathbf{x}_t|\mathbf{y})}{\sigma_t^2} \left[\mathbb{E}[\mathbf{x}_0|\mathbf{x}_t, \mathbf{y}] - \mathbf{x}_t \right] \\ \frac{\nabla_{\mathbf{x}_t} p_t(\mathbf{x}_t|\mathbf{y})}{p_t(\mathbf{x}_t|\mathbf{y})} &= \frac{1}{\sigma_t^2} \left[\mathbb{E}[\mathbf{x}_0|\mathbf{x}_t, \mathbf{y}] - \mathbf{x}_t \right]. \end{aligned}$$

We note that from our assumption, $p_t(\mathbf{x}_t|\mathbf{y})$ is fully supported everywhere, so we avoid singularities when dividing by this quantity.

Finally, we again invoke the identity $\nabla_x \log f(x) = \nabla_x f(x)/f(x)$ to rewrite the left-hand side and rearrange to obtain the desired result:

$$\begin{aligned}\nabla_{\mathbf{x}_t} \log p_t(\mathbf{x}_t|\mathbf{y}) &= \frac{1}{\sigma_t^2} \left[\mathbb{E}[\mathbf{x}_0|\mathbf{x}_t, \mathbf{y}] - \mathbf{x}_t \right] \\ \mathbb{E}[\mathbf{x}_0|\mathbf{x}_t, \mathbf{y}] &= \mathbf{x}_t + \sigma_t^2 \nabla_{\mathbf{x}_t} \log p_t(\mathbf{x}_t|\mathbf{y}).\end{aligned}$$

□

B Extended Experimental details

B.1 Dataset

All MRI data are initially stored as complex-valued multi-coil k-space measurements. We appropriately crop the raw k-space data and MVUE images for brain scans to 384×384 pixels and knee scans to 320×320 pixels for all experiments.

For training the score network on brain scans, we take volumes from the fastMRI multi-coil brain training set and remove the last two noisy slices from each volume for a total of 57,297 scans. For training on knee scans, we keep all data in the fastMRI multi-coil knee training set for a total of 28,102 scans. We use brain and knee scans from all available contrasts and field strengths for training the score networks. To make the data compatible with real-valued network weights, we represent the complex-valued MVUE images as two-channel, real-valued images.

Since the data exhibit a wide dynamic range of pixel values, we linearly scale images to the range $[-1, 1]$ when training the score networks using the minimum and maximum pixel values from the two-channel fully-sampled MVUE images. When learning sampling patterns and performing posterior sampling, we use the minimum and maximum pixel values from the MVUE calculated from the retrospectively-undersampled k-space data to perform this scaling.

For training and evaluating sampling patterns, we use T2-weighted brain scans and proton density-weighted knee scans without fat suppression, all with a field strength of 3 Teslas. We remove the first ten slices from knee volumes and last five slices from brain volumes when creating the training, validation, and test sets for learning sampling patterns with our method.

B.2 Training Diffusion Models

We train score-based networks using the ADM architecture [14] and the default parameters for ImageNet 256 with some changes. We use 128 base channels instead of 256 and self-attention in the two smallest resolution scales instead of three smallest. The models are trained with classifier-free diffusion guidance [23] with a label dropout probability of 0.1, treating each unique (contrast, field strength) pair as a different class. We train one network for brain scans and one for knees.

B.3 Training Sampling Patterns

When training the sampling patterns using Eq. (15), we use a single forward operator $\mathcal{A}(\mathbf{x}) = \mathbf{P}\mathbf{F}\mathbf{x}$ instead of using $\mathcal{A}_i(\mathbf{x}) = \mathbf{P}\mathbf{F}\mathbf{S}_i\mathbf{x}$ for each of the c coils with $i \in [c]$. In other words, we do not use the coil sensitivity maps \mathbf{C}_i when retrospectively sub-sampling training data to create measurements. We find that this method accelerates training by avoiding memory and computational costs for multiple coils. We also find that this method improves test performance and leads to more stable convergence of the learned sampling patterns. During validation and testing, we still perform reconstructions using undersampled multi-coil k-space data as measurements.

During validation, we perform posterior sampling to reconstruct each image in the validation set and track the error between the reconstructions and fully-sampled images. Before testing, we restore the weights of the sampling operator from the iteration with the lowest mean validation error.

B.4 Hyperparameters

We tune the following hyperparameters: the training likelihood step size γ , Gumbel temperature τ , learning rate for sampling patterns, sampling likelihood step size ρ , and sampling stochasticity parameter S_{churn} .

For the general experiments in Figures 1 and 2, we fix the number of sampling steps to 100 and search for the values of $\rho \in \{0.1, 0.2, \dots, 1, 2, \dots, 10\}$ and $S_{churn} \in \{0, 10, \dots, 50\}$. We choose the pair of values with the smallest reconstruction error on a hold-out set of 30 scans. Once we find the optimal values $\rho = 10$ and $S_{churn} = 0$, we fix them and search for values of $\gamma \in \{0.1, 0.5, 1, 5, 10\}$ and $\tau \in \{0.1, 0.5, 1\}$. We train sampling patterns for 2 epochs on our training set using a learning rate of 0.1 and choose the pair $\gamma = 1$ and $\tau = 1$ that gives the best reconstruction error on the 30 hold-out scans using the learned pattern. Finally, we fix all previous tuned hyperparameters and search for the learning rate in $\{10^{-4}, 10^{-3}, 10^{-2}, 10^{-1}\}$ by again training for 2 epochs and reconstructing hold-out

images, finding 10^{-2} to be optimal. We tune all listed hyperparameters using 2D patterns with $R = 4$ on brain scans and use the same values across all anatomies, pattern types, and accelerations.

For the experiment in Figure 3 (b), we set $S_{churn} = 0$ and set $\rho = 20$ for 25 steps, $\rho = 10$ for 100 steps, $\rho = 8$ for 200 steps, $\rho = 6$ for 400 steps, $\rho = 4$ for 600 steps, $\rho = 3$ for 800 steps, and $\rho = 2$ for 1000 steps. To tune these values, we start from 25 steps and search for $\rho \in \{1, 2, \dots, 25\}$ and notice that the optimal value $\rho = 20$ is larger than for 100 steps ($\rho = 10$). Continuing, as we find the optimal ρ for each step value, we increase the number of steps and restrict the search space to smaller and smaller subsets, with the maximum search value being the optimal value of ρ for the previous step value. For example, we search $\rho \in \{1, 2, \dots, 10\}$ for 200 steps and $\rho \in \{1, 2, \dots, 8\}$ for 400 steps. For the experiment in Figure 3 (c), we re-use the optimal value of $\rho = 2$ for 1000 steps. We fix the same value $\rho = 2$ for all values of S_{churn} in this experiment. We tune the hyperparameters for these experiments on a hold-out set of 30 brain scans with 2D patterns and $R = 10$.

C PSNR Plots

In this section we present PSNR plots for the experiments from Figures 2 and 3.

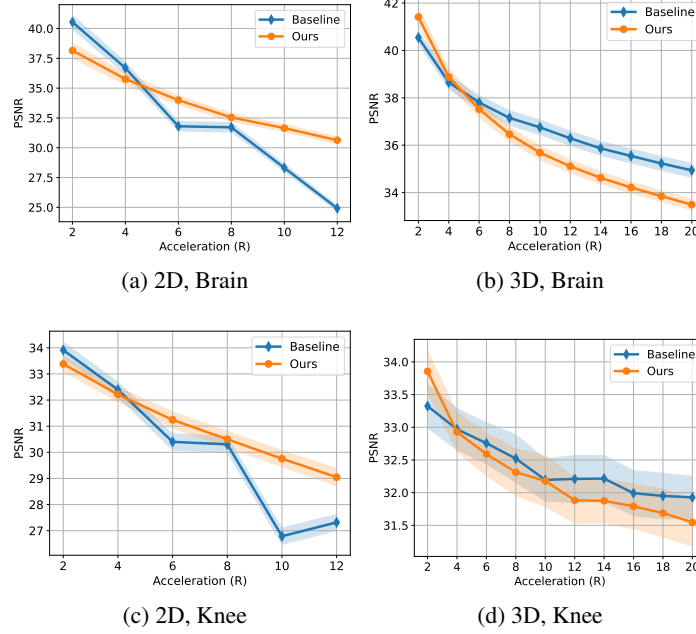


Figure 5: **Mean test PSNR for 2D and 3D patterns on Brains and Knees.** We compare reconstructions with masks learned using our method to those with fixed baseline masks across a range of acceleration factors. The shaded areas indicate a 95% confidence interval.

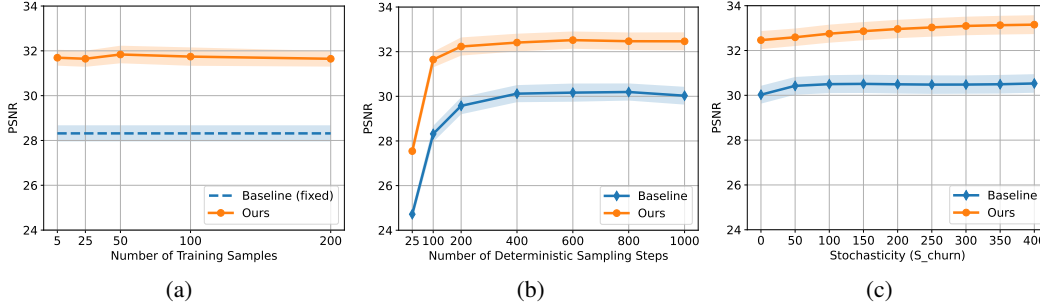


Figure 6: **Test results for varying training and sampling parameters.** We vary (a) the number of training samples for our method, (b) the number of deterministic sampling steps, and (c) the stochasticity of sampling for 1000 steps (determined by S_{churn} as in Algorithm 1), and present the mean PSNR on the test set. The shaded areas indicate a 95% confidence interval. All experiments are performed on brain scans using 2D patterns with an acceleration of $R=10$.

D Additional Plots of Learned Masks and Reconstructions

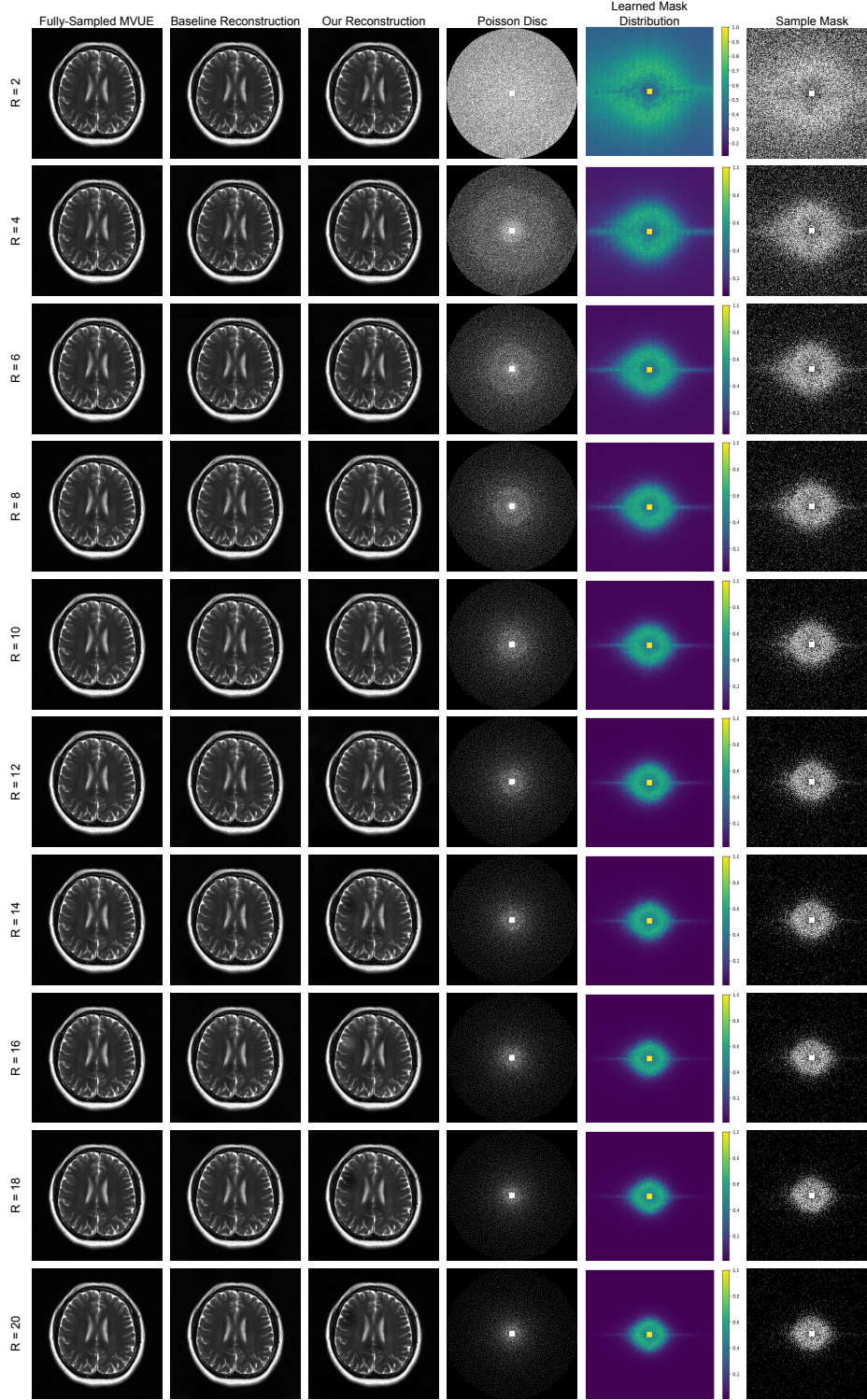


Figure 7: **Learned 3D Sampling Patterns and Reconstructions for Brains.** We perform posterior sampling using a diffusion model to reconstruct brain scans for varying acceleration factors (R) using 3D patterns. We colorize the probability distributions of our learned patterns for easier viewing.

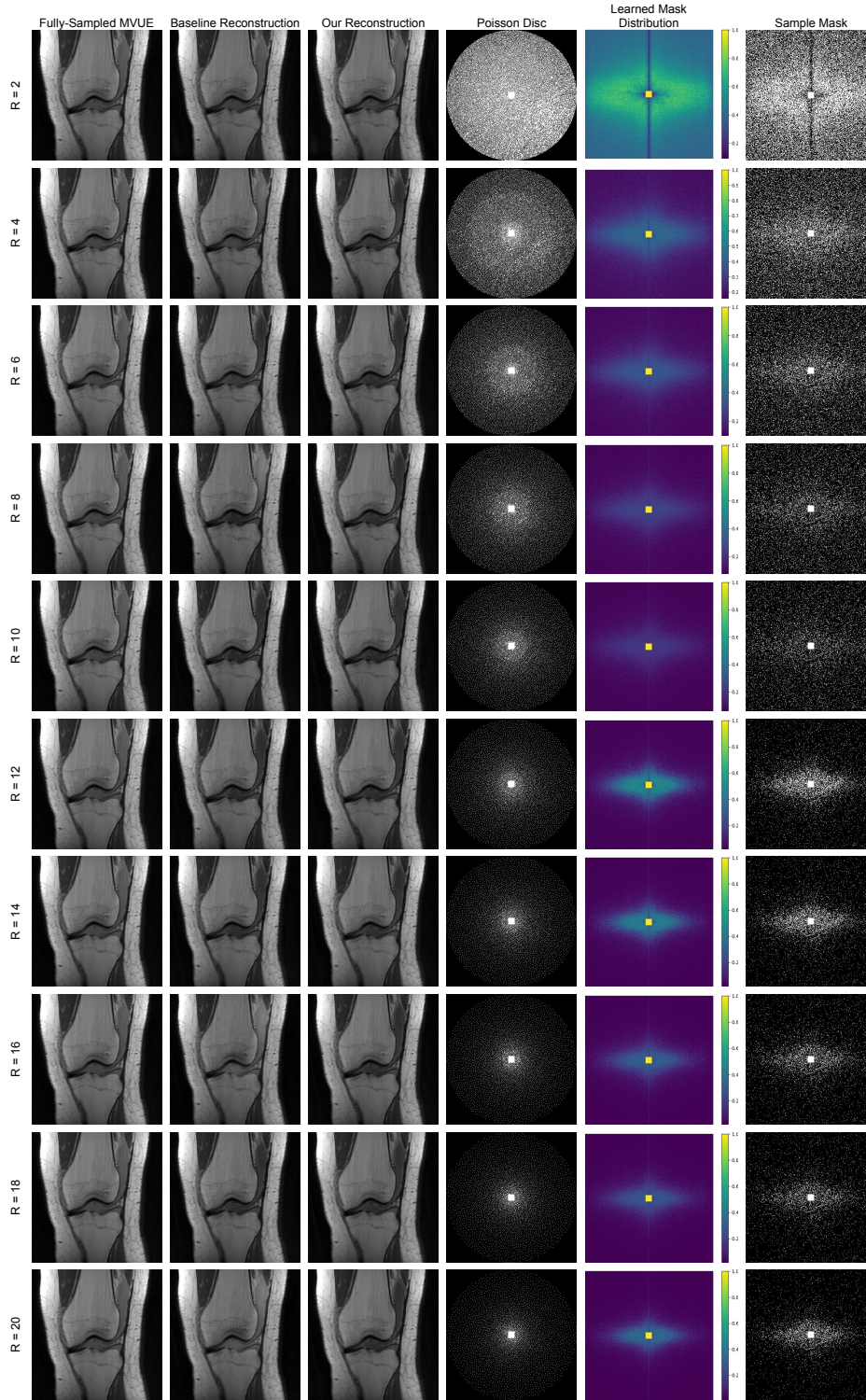


Figure 8: **Learned 3D Sampling Patterns and Reconstructions for Knees.** We perform posterior sampling using a diffusion model to reconstruct knee scans for varying acceleration factors (R) using 3D patterns. We colorize the probability distributions of our learned patterns for easier viewing.

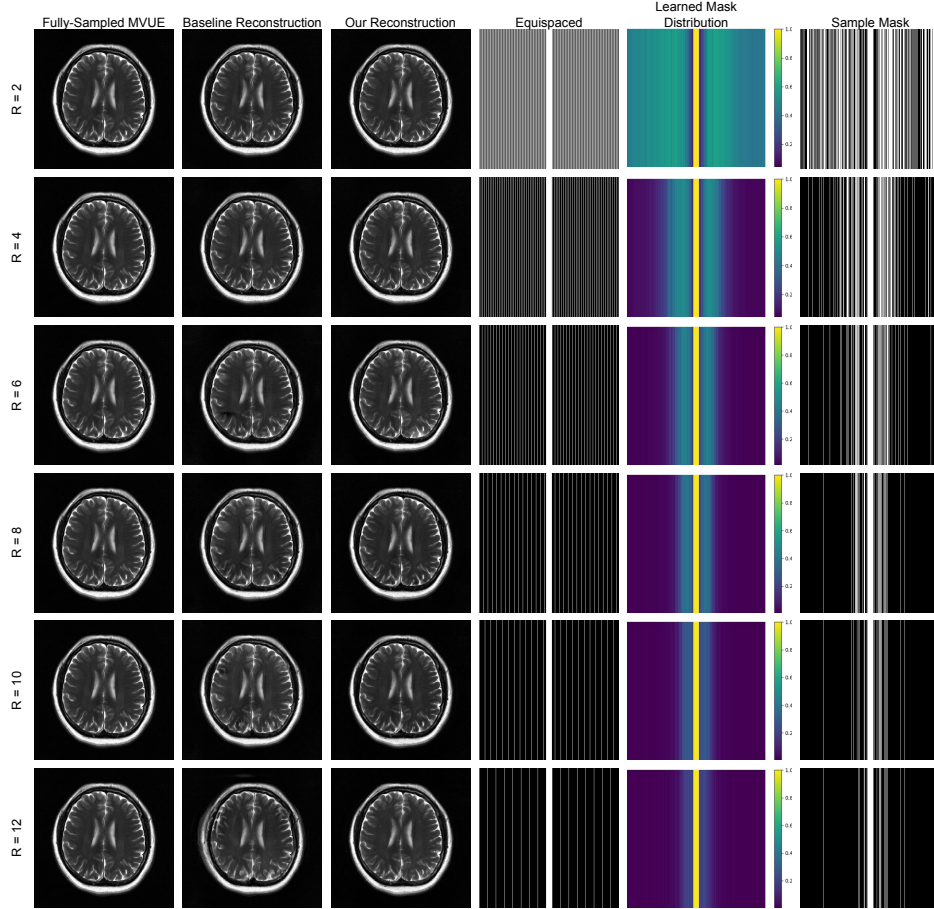


Figure 9: **Learned 2D Sampling Patterns and Reconstructions for Brains.** We perform posterior sampling using a diffusion model to reconstruct brain scans for varying acceleration factors (R) using 2D patterns. We colorize the probability distributions of our learned patterns for easier viewing.

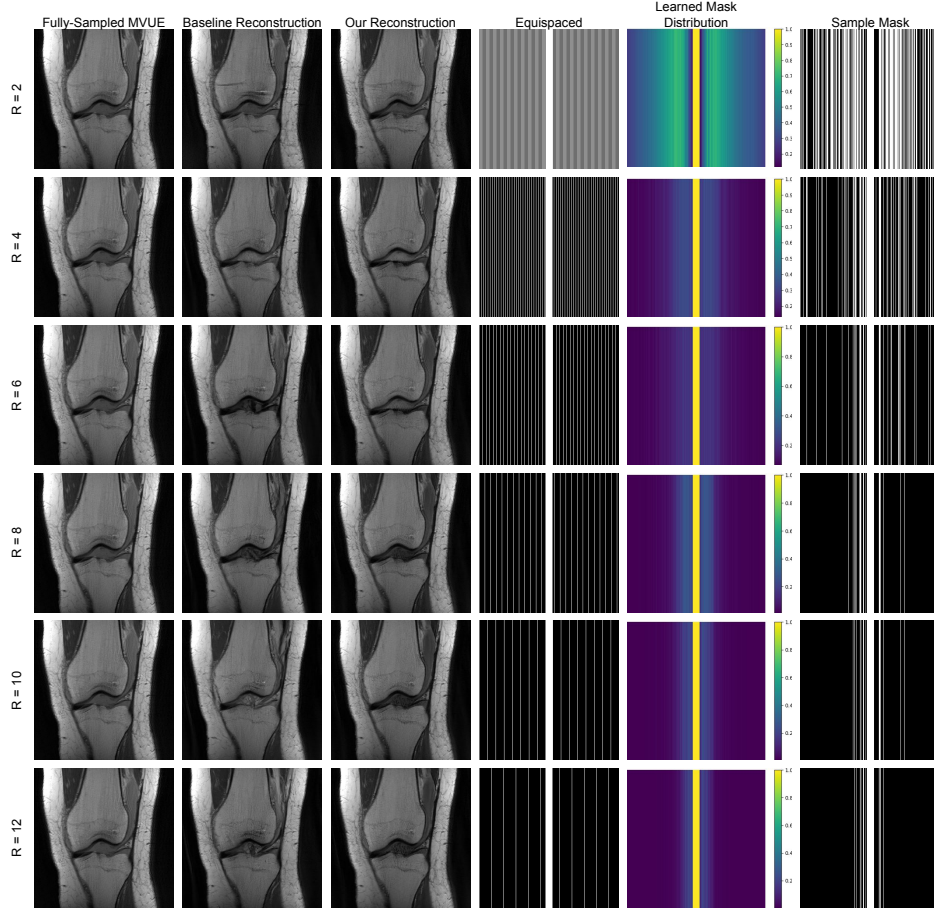


Figure 10: **Learned 2D Sampling Patterns and Reconstructions for Knees.** We perform posterior sampling using a diffusion model to reconstruct knee scans for varying acceleration factors (R) using 2D patterns. We colorize the probability distributions of our learned patterns for easier viewing.